Scientific paper

Shear Behaviour of Full-Scale Squat Shear Walls with and without Precast Pre-walls

Eissa Fathalla[1*], Bertrand Ringeisen[2], Marc Lenges[3] and Boyan Mihaylov[4]

Received 7 November 2023, accepted 8 February 2024 doi:10.3151/jact.22.86

Abstract

Reinforced concrete shear walls are commonly used in buildings to resist lateral loads due to wind and seismic action. They are typically either cast-in-place or precast, with the latter solution used to achieve high construction speed and quality control. At the same time, the main challenge with precast solutions is to ensure appropriate connections between the adjacent walls, as well as the anchorage of the walls in the foundations. A hybrid structural system combining precast and cast-in-place concrete can provide the advantages of both methods such as faster construction, better quality control, improved structural performance, and durability. This study focuses on investigating the shear behaviour of squat hybrid shear walls through full-scale experimental testing. The tests include one conventional cast-in-place wall and one hybrid wall with a pre-wall system (two precast walls) and cast-in-place concrete core. Detailed measurements and kinematic-based modelling are used to develop comprehensive understanding of the behaviour of the test specimens. It is shown that the hybrid method of construction does not affect the stiffness of the walls and results in a slight reduction of shear strength. It is also shown that the three-parameter kinematic theory can be used to predict the shear strength and key deformation components of the tested walls.

1. Introduction

Reinforced concrete (RC) shear walls are a common structural system for medium to high-rise buildings to resist lateral loads due to wind and seismic action. The conventional method for constructing shear walls is through monolithic casting. However, precast concrete has gained popularity in the past decades due to its advantages in construction speed and quality control (Kurama *et al.* 2018; Negro *et al.* 2013). At the same time, one of the most significant challenges in using precast concrete walls is ensuring the proper connections between the precast units, as well as between the walls and the foundation. These connections are crucial in determining the behaviour of the walls, including their lateral stiffness, strength, and ductility. Proper design and construction practices for these connections are essential for ensuring the safety of precast concrete wall systems in seismic regions (Magliulo *et al.* 2014; Grimaz *et al.* 2010; Toniolo and Colombo 2012; Yin *et al.* 2009; Huixian *et al.* 2002; Saatcioglu *et al.* 2001).

A solution to this connection problem is the use of a hybrid structural system with a pre-wall system that combines the benefits of cast-in-place concrete and precast construction methods. In this system, the main shear reinforcement is included in two external walls of the pre-wall system, which are precast and linked with steel connectors. On the construction site, the pre-wall systems are used as formwork to cast the core of the wall. Linking reinforcement and additional flexural reinforcement is provided in the cast-in-place core. Thus, the outer precast walls typically act as the primary lateral load-resisting elements, while the cast-in-place core accommodates the anchorage to the foundation and provides additional stiffness and strength to the system. This system offers several advantages, including faster construction with minimum formwork, higher quality control, durability, and increased structural performance during seismic events. Moreover, considering the important environmental challenges, there is a need to reduce the carbon dioxide footprint of shear wall structures (Adesina 2020). In the hybrid solution, this can be achieved by introducing voids in the inner core (subtracting concrete) without a significant impact on the strength and stiffness of the wall.

The main question regarding hybrid walls with a pre-wall system pertains to the effectiveness of the composite action of the pre-wall system and the core concrete. While conventional cast-in-place walls have been extensively studied (Greifenhagen and Lestuzzi 2005; Hannewald *et al.* 2013; Hirosawa 1975; Ji *et al.* 2018; Lefas

[1]Assistant Professor, Structural Engineering Department, Cairo University, Giza 12613, Egypt, and Urban and Environmental Research Unit (UEE), University of Liège, Building B52, Quartier Polytech 1, Allée de la Découverte 9, B-4000 Liège, Belgium.
*Corresponding author,
E-mail: mmeissa@uliege.be
[2]Research and Development Engineer, Spurgin Leonhart, Route de Strasbourg BP 20151, 67603 Selestat Cedex, France.
[3]Technical Director, Spurgin Leonhart, Route de Strasbourg BP 20151, 67603 Selestat Cedex, France.
[4]Associate Professor, Urban and Environmental Research Unit (UEE), University of Liège, Building B52, Quartier Polytech 1, Allée de la Découverte 9, B-4000 Liège, Belgium.

et al. 1990; Lopes 2001; Luna *et al.* 2015; Luna 2016), there is a lack of experimental studies that directly compare the behaviour of such conventional elements to hybrid walls with a pre-wall system. Therefore, it is the goal of this paper to provide such a direct comparison through two full-scale laboratory tests: one conventional wall and one wall with a pre-wall system with a length of 2.2 m. The specimens were squat with an aspect ratio of approximately 1.0 and featured a T-section with a tension flange. They were designed to develop large diagonal compressive stresses across the web in order to test the composite action of precast and cast-in-place concrete. Detailed deformation measurements were conducted using displacement transducers and full-view digital image correlation (DIC) of the walls. The measured deformations are used to develop a comprehensive understanding of the walls. The study also shows how the three-parameter kinematic theory (3PKT) (Mihaylov *et al.* 2016; Fathalla and Mihaylov 2022) for conventional shear-critical walls with rectangular sections can be extended to predict the shear strength and important deformations of conventional and hybrid walls with tension flanges.

2. Experimental program

2.1 Test specimens

Figure 1 shows the two T-shaped specimens of the experimental study: the conventional cast-in-place wall W1 and the hybrid wall with a pre-wall system W2. The external design dimension of the two walls were identical. The web of wall W2 was constructed with two 2000×2000 mm precast walls (one on each side), each of which with a thickness b_p of 50 mm. The two precast walls of the pre-wall system were linked with vertical truss-type steel connectors as shown in **Fig. 2(b)**. The concrete core between the precast walls, as well as the flange of wall W2, were cast in place and contained additional vertical (flexural) reinforcement.

The aspect ratio of the walls *a/h* is 1.02, the height subjected to shear a is 2250 mm, the clear height a_{cl} is 2000 mm, the total length of the section h is 2200 mm, the web thickness b is 200 mm (precast walls and core for W2), the thickness of the cast-in-place core b_c is 100 mm, and the flange width B_f (tension side) is 800 mm with a thickness t_f of 200 mm. These design dimensions were respected in the construction of the walls, with the exception of the flange width of wall W1 which was built wider than specified at 940 mm.

The reinforcement of the two test specimens is shown in **Fig. 2**. Each precast wall of specimen W2 was reinforced with a ⌀6/150 mm steel mesh in the vertical direction (reinforcement ratio of 0.19% on the basis of the total concrete section of the web of the wall) and a ⌀6/100 mm steel mesh in the horizontal direction (reinforcement ratio of 0.28%). The core between the precast walls accommodated splicing vertical reinforcement coming from the top and bottom concrete blocks, as well as six ⌀20 mm bars on the flexural compression side of the section. The tension flange was reinforced heavily with sixteen ⌀20 mm bars anchored with hooks in the bottom block, and with lap-spliced U-shaped bars in the top block. For the purpose of direct comparisons, the reinforcement of the cast-in-place wall W1 was kept the same as that of W2 (**Fig. 2**). In both walls, the clear concrete cover of the reinforcement was 30 mm.

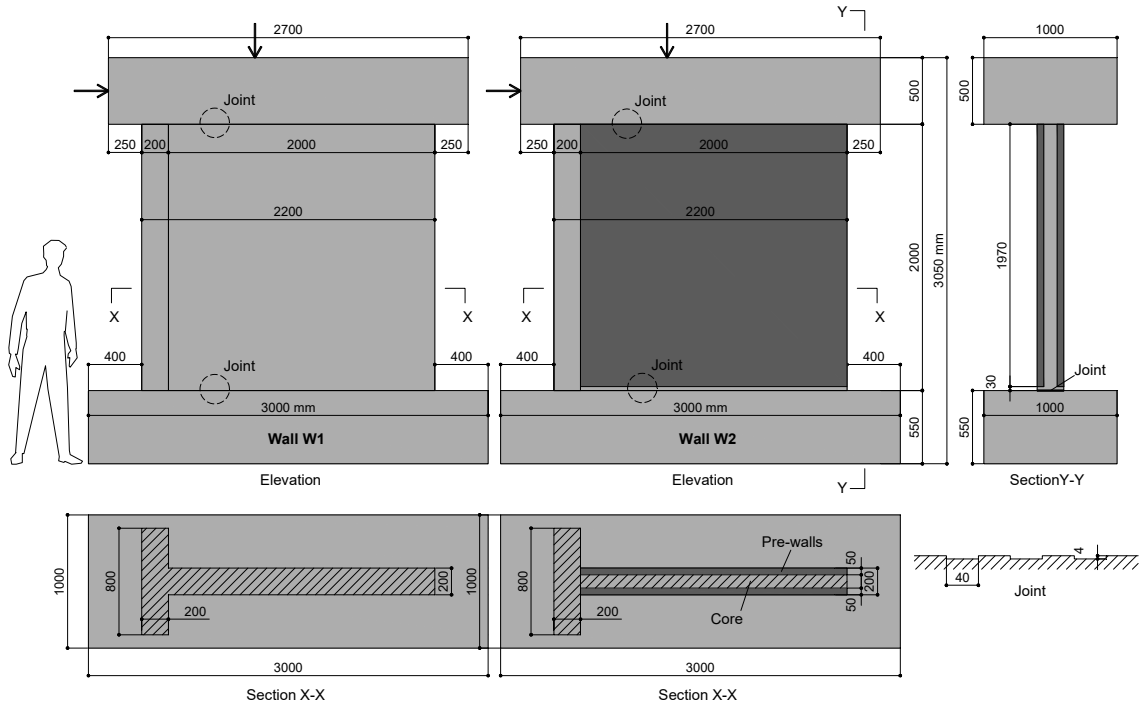

Fig. 1 Design geometry of the tested shear walls.

Table 1 Concrete material properties of shear walls.

Wall	Concrete layer		Compressive strength f_c (MPa)	Strain at peak stress ε_{c1} (‰)	Modulus of elasticity E_c (MPa)	Concrete age (Days)
W1	One		51.7	2.7	29250	453
W2	Pre-wall	Face 1	51.3	2.6	30550	356
		Face 2	51.4	2.3	33080	354
	Core		52.1	3.0	29620	341

Note: The equivalent concrete strength of W2 is 51.8 MPa (weighted average based on each component thickness).

2.2 Material properties

2.2.1 Concrete

The concrete of wall W1 was cast in place from a single batch, and three 300 mm by 150 mm cylinders were cast for material testing. For wall W2, each concrete component was cast from a different batch (two precast walls and a cast-in-place core); thus, three cylinders of each concrete component were cast for material testing. The type of coarse aggregates for precast walls and cast-in-place concrete was gravel with a maximum size a_g of 16 mm.

For material characterization, cylinder compression testing was conducted. One cylinder for each concrete component was tested with strain measurements to obtain the complete pre-peak stress-strain response, including important properties such as the modulus of elasticity E_c, strain at peak stress ε_{c1}, and concrete strength f_c. The other two cylinders were tested to obtain the concrete strength only.

Table 1 shows the results from the cylinder tests of the different concrete components of the shear walls, in addition to the age of the concrete at the time of testing. The concrete strength f_c is obtained as the average of the three cylinders. The stress-strain response of each component is shown in **Fig. 3**. It can be seen that all components exhibited a similar behaviour, with f_c varying slightly between 51.3 and 52.1 MPa.

2.2.2 Reinforcement

To obtain the stress-strain response of the steel reinforcement, one standard coupon test was performed for each bar diameter. A summary of the test results is presented in **Table 2**. The yield strength of the reinforcement f_y varied between 514 MPa and 563 MPa, and the rupture strain ε_u between 60‰ and 93‰.

2.3 Test setup

Figure 4 shows the test setup used for the loading of specimens W1 and W2 via the stiff top and bottom concrete blocks of the walls. The bottom block acts as a foundation, which is post-tensioned to the strong floor of the lab via Dywidag bars to prevent uplift and sliding during the lateral loading. The top block acts as a loading beam that distributes uniformly the applied vertical load on the wall. To simulate gravity loads, a vertical (axial) load N of 700 kN was applied on the top block via a steel assembly and 2 Dywidag bars, one on each side of the wall. These bars were pulled down from underneath the strong

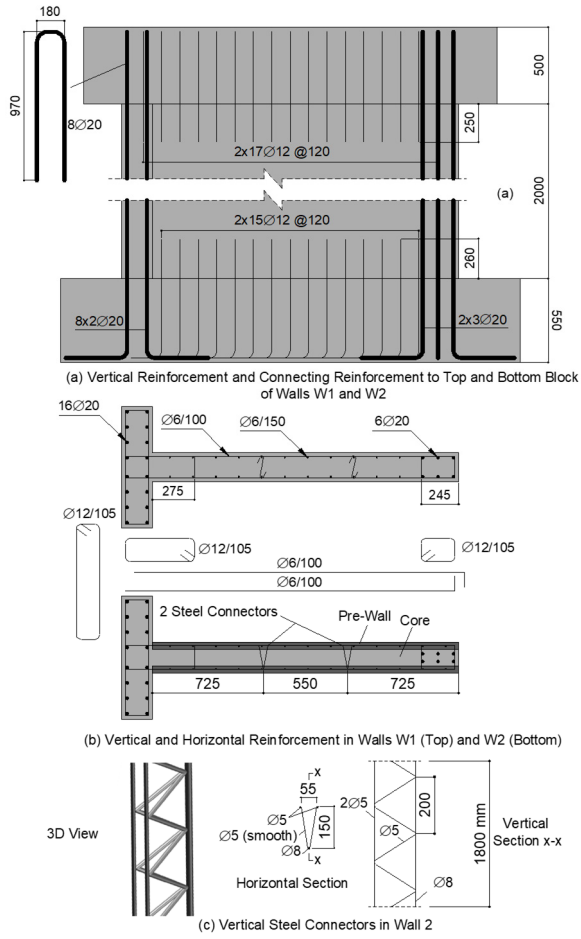

Fig. 2 Reinforcement details of tested shear walls.

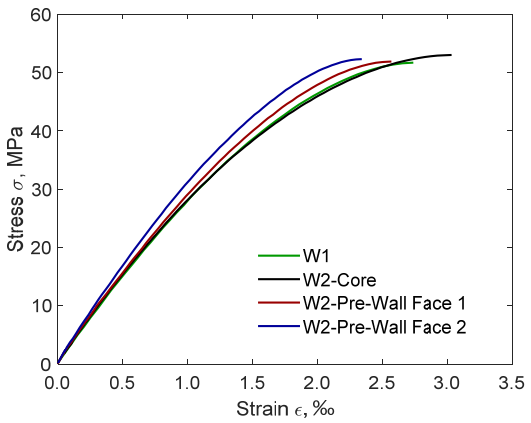

Fig. 3 Stress-strain curves of the concrete of the tested walls.

Table 2 Properties of steel reinforcement.

Nominal diameter	Yield strength	Ultimate strength	Modulus of elasticity	Yield strain	Rupture strain
mm	f_y (MPa)	f_u (MPa)	E_s (MPa)	ε_y (‰)	ε_u (‰)
12	544	627	199800	2.72	78
20	563	645	207400	2.71	60
6	514	626	192100	2.67	93

Note: The rebar sample of 6 mm diameter was not obtained from the batch used for the walls, but from another batch of the same manufacturer.

floor by hydraulic jacks. The vertical load was applied approximately at the centroidal axis of the gross concrete section of the walls to ensure constant compressive stresses across the T-section.

The lateral load was applied with two hydraulic jacks with hinges at the ends. The out-of-plane stability of the walls was ensured by two steel frames equipped with low-friction pads at the contact points between the frames and the top concrete block. The frames were placed on the flexural compression side of the walls, opposite to the side of the flange. After the application of the vertical load, it was kept constant, and the walls were loaded with a lateral load at the centre of the top concrete block. The load was applied monotonically in load control (1 to 3 kN/s) in several load steps up to the failure of the wall. After each load step, the load was reduced by 10% and kept constant in order to perform crack width measurements and take photos for reporting.

2.4 Instrumentation

In order to measure global and local deformations, 14 displacement transducers (DTs) were installed at one side of the wall as shown in **Fig. 5**. Transducers DT1 and DT2 are used to measure the horizontal displacement at the centre of the top block with respect the bottom concrete block (global drift), DT3 and DT4 are used to measure the vertical displacement and rotation of the top block, DT5 is used to measure the horizontal displacement at 600 mm from the base of the wall on the flexural compression side, DT6 measures the base crack opening at the web, DT7 measures the base crack opening at the flange, diagonal transducers DT8 and DT9 are used to measure the global shear deformation of the wall, DT10 and DT11 are used to monitor the rotation of the bottom block (if it occurs), DT12 is used to measure the slip of the bottom block with respect to the strong floor (if it occurs), DT13 is used to measure the local horizontal web expansion at the centre of the wall, and DT14 is used to measure the slip between the base of the wall and the bottom block (construction joint). Finally, the vertical load N and horizontal lateral load V on the specimens were measured based on the pressure in the hydraulic machine, which was calibrated before the tests.

Additionally, 3D digital image correlation (DIC) technique is utilized on the entire opposite face of the walls. The DIC aims to obtain detailed displacement and strain measurements across the entire face by post-processing of photos taken by a pair of 24-megapixel cameras during the test. The post-processing was conducted by using the software VIC-3D (Correlated Solutions 2023). It should be noted that the DIC results were validated with the measurements from the displacement transducers on the opposite side of the walls (i.e., DT13). As shown in **Fig. 10** in the following section, the DIC results (thin lines) were consistent with the DT13 measurements.

Fig. 4 Test setup of shear walls.

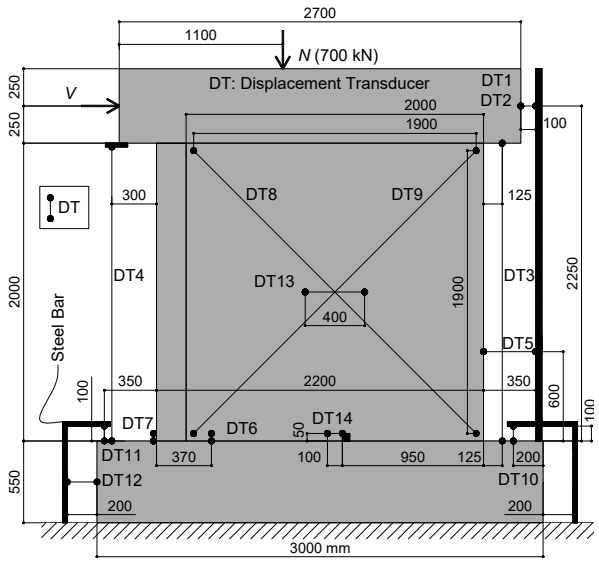

Fig. 5 Instrumentation of shear walls.

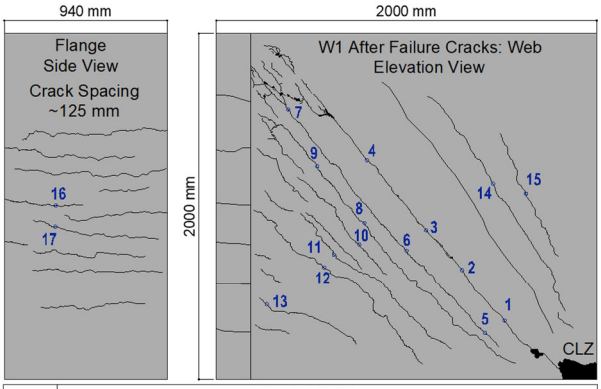

Point	Crack Width, mm Load Level V/V_u, %									
	21	28	35	42	48	55	62	69	76	100
1	–	–	–	–	–	–	–	–	0.42	1.54
2	–	–	–	–	–	–	–	–	0.74	1.87
3	–	–	–	–	–	–	–	–	1.13	1.94
4	–	–	–	–	–	–	–	–	0.88	2.00
5	–	–	–	–	–	–	0.16	0.24	0.28	0.43
6	–	–	–	–	–	–	0.34	0.55	0.69	0.90
7	–	–	–	–	–	–	0.30	0.41	0.61	0.85
8	–	–	–	–	0.19	0.45	0.59	0.60	0.61	0.62
9	–	–	–	–	0.43	0.54	0.59	0.63	0.66	0.77
10	–	–	–	–	0.30	0.38	0.40	0.42	0.43	0.50
11	–	–	0.24	0.34	0.37	0.43	0.44	0.44	0.46	0.46
12	–	–	0.27	0.28	0.29	0.31	0.32	0.37	0.42	0.42
13	–	0.12	0.16	0.17	0.24	0.39	0.41	0.44	0.46	0.55
14	–	–	–	–	–	–	–	0.30	0.35	0.44
15	–	–	–	0.27	0.27	0.32	0.34	0.35	0.35	0.38
16	0.05	0.06	0.10	0.13	0.20	0.22	0.24	0.31	0.33	0.38
17	–	–	0.10	0.15	0.15	0.16	0.20	0.20	0.24	0.35

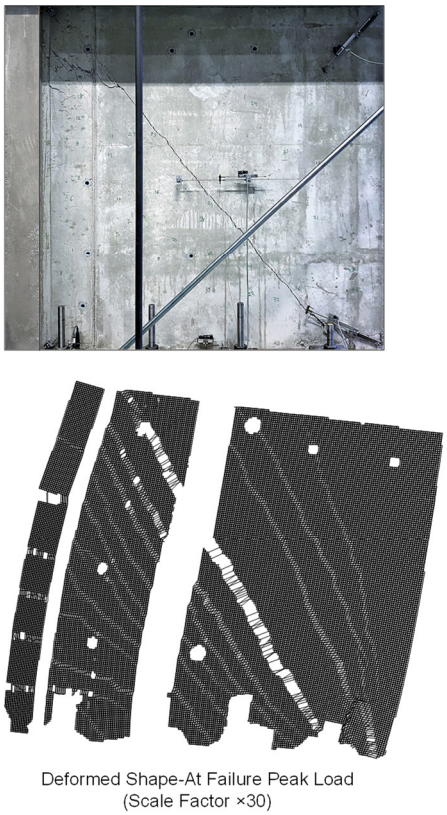

Fig. 6 Crack pattern (major cracks) of wall W1 after failure, crack widths at various load levels, and deformed shape at peak load.

3. Experimental results

3.1 Wall W1

Wall W1 failed in brittle shear at a lateral load (shear force) V_u=2599 kN and a top lateral displacement Δ_u=13.0 mm (drift Δ_u/a= 0.58%). As shown in **Fig. 6**, the failure occurred with opening of a critical shear crack along the diagonal of the wall, as well as crushing of the concrete in the compressive "toe" of the wall. In the following discussion and modelling, the zone of crushed concrete will be referred to as the critical loading zone (CLZ). **Figure 6** also shows the widths of the cracks at various locations across the web and along the flange, measured at several load levels V/V_u up to failure. The maximum width of the shear and flexural cracks reached ≈2.0 mm and ≈0.40 mm at failure (V/V_u=100%), respectively. The deformed shape at failure is obtained from the DIC measurements as also shown in the figure. It can be seen from this diagram that the critical diagonal crack separated the wall into two regions: a block with relatively small deformations above the crack, and a region marked by a "fan" of flexural-shear cracks below the critical crack.

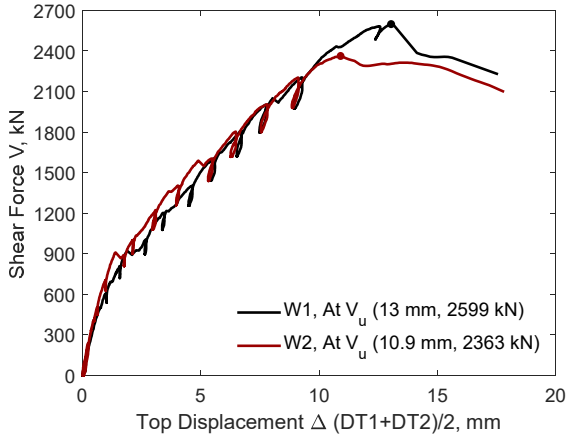

Fig. 7 Global behaviour of walls W1 and W2.

Figure 7 shows the complete global response of wall W1 in terms of lateral load V versus top lateral displacement Δ. In parallel, the development of the cracks with increasing lateral load is shown in **Fig. 8**, using the principle tensile strains ε_1 obtained from the DIC measurements. The wall behaved linearly up to a load of ≈600 kN (≈23%V_u) when the first cracks occurred in the bottom of the flange, and the construction joint at the base began to open. At approximately the same load, inclined flexural-shear cracks also developed in the vicinity of the flange cracks, and a slight reduction in the stiffness was observed. The flexural-shear cracks remained stable without the formation of new cracks up to V≈800 kN (≈31%V_u). By increasing the load further, new flexural cracks developed in the flange, as well as new flexural-shear cracks in the web. The cracking spread upwards in

the flange and towards the diagonal of the wall in the web. The tangent stiffness was lower than the initial stiffness but remained approximately constant until V≈2050 kN (≈79%V_u), when the critical diagonal crack formed. After this point up to the failure load, the critical diagonal crack widened with a corresponding gradual decrease of the tangent stiffness. Finally, the failure occurred by crushing of the critical loading zone (CLZ) and rapid opening of the critical diagonal crack. Three inclined cracks above the critical crack had penetrated in the CLZ before failure.

The behaviour of wall W1 is further illustrated with local deformation measurements in **Figs. 9** to **11**. The opening of the construction joint in the base of the wall in **Fig. 9** is associated mainly with the penetration of strains along the anchorage of the vertical reinforcement in the foundation block. The opening at the external edge of the flange reached 0.83 mm at failure, while that in the web had a maximum value of 0.40 mm. No plastic plateau is observed in the opening of the base joint, which signifies that the flexural reinforcement did not yield. This is also consistent with the small horizontal displacement measured across the construction joint: a value of 0.13 mm was recorded by DT14 at failure as shown in **Fig. 11**. As displacement transducer DT14 was placed at 50 mm above the base, its reading comes in part from shear strains in the uncracked concrete immediately above the joint. The average shear strain γ can be estimated from the two diagonal transducers DT8 and DT9 as ≈($|\varepsilon_1|+|\varepsilon_2|$), where ε_1 is the principal tensile strain calculated from DT9, and ε_2 is the principal compressive strain calculated from DT8. The calculated shear strain at failure is 3.8×10^{-3}. When this value is multiplied by 50 mm, it produces a displacement of 0.18 mm, which is close to the measurement of DT14. This shows that, even though W1 was squat, the slip displacement in the construction joint was negligible.

Compared to the horizontal displacement in the base joint, the horizontal displacement measured by DT13 in the centre of the web was significant (**Fig. 10**). Transducer DT13 was placed to capture the horizontal opening of the critical diagonal crack. It can be seen that the crack did not form until V≈2050 kN (≈79%V_u), and rapidly reached a value of 1.6 mm at failure. This value is clearly sufficient to yield the horizontal web reinforcement with bar diameter of 6 mm.

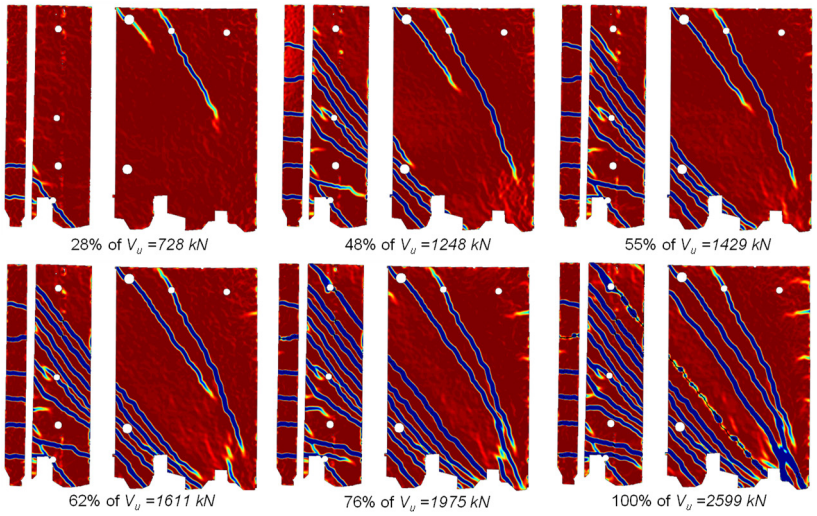

Fig. 8 Contour map of principal tensile strain ε_1 from post-processing of DIC measurements of wall W1.

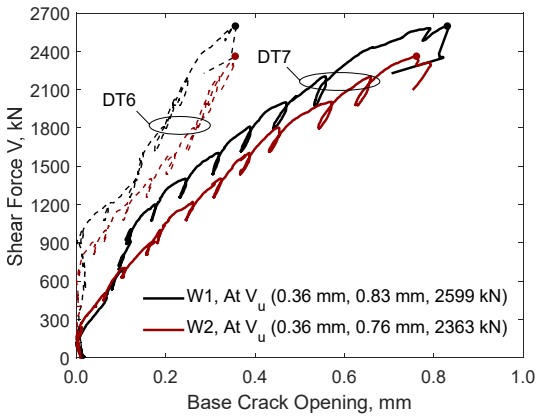

Fig. 9 Measured base crack/joint opening in walls W1 and W2.

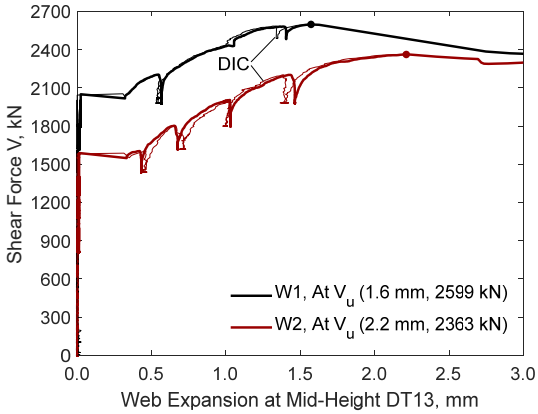

Fig. 10 Measured web expansion in walls W1 and W2.

The horizontal displacement in the critical crack is associated with the shearing and crushing of the CLZ at the bottom of the crack. In squat walls such as W1, the CLZ carries significant shear by means of inclined compression, and therefore it is of interest to evaluate the compressive strains of this region. **Figure 12** shows the contour map of the principal compressive strain ε_2 in wall W1 obtained from the DIC measurements at failure. This map clearly highlights the CLZ, where high strains localized. The maximum stains in the CLZ exceeded 3.0 ‰ at failure, which is consistent with the observed crushing of concrete in this zone.

3.2 Effect of pre-wall system: Wall W2

The behaviour of wall W2 is compared to that of W1 to evaluate the effect of the pre-wall system used in the construction of the former wall. As shown by the crack diagram and deformed shape in **Fig. 13**, the failure of W2 was remarkably similar to that of W1. It occurred with the opening of a critical diagonal crack and simultaneous crushing of the concrete in the CLZ. The failure lateral load was V_u=2363 kN and the corresponding top lateral displacement was Δ_u=10.9 mm (drift of 0.48%). Therefore, the wall with a pre-wall system had a 9.1% lower strength and 16.2% smaller displacement capacity than the conventional wall built with cast-in-place concrete. The crack widths at failure were also similar to those of W1: the critical diagonal crack reached ≈2.2 mm (vs. ≈2.0 mm in W1), while the maximum crack width in the flange was ≈0.4 mm (same as in W1).

Figure 7 compares the complete global response of wall W2 (solid line) to that of wall W1 (dashed line) in terms of lateral load V versus top lateral displacement Δ. The two responses are almost overlapping until the failure of W2. A small difference is observed in the load range V=600-1600 kN where the wall with a pre-wall system was slightly stiffer. Wall 2 behaved linearly up to a load of ≈900 kN (≈38%V_u) when flexural and flexural-shear cracks occurred in the flange and web, respectively see (**Fig. 14**). As before, further loading caused the cracking to spread upwards along the flange and towards the diagonal of the wall in the web. The critical diagonal crack in W2 formed at a load of ≈1600 kN (≈67%V_u), which is significantly earlier than in W1 (2050 kN). No other cracks formed after the critical diagonal crack, and the response of wall W2 became slightly nonlinear until failure. In addition, there were no major cracks above the diagonal of the wall, which was a noteworthy difference with the cracks observed in the cast-in-place wall – compare **Fig. 14** with **Fig. 8**.

The local deformations of W2 are compared to those of W1 in **Figs. 9** to **11**. The opening of the base joint of W2 was almost identical to that of W1 at failure: 0.76 mm at the flange and 0.40 mm at the web **(Fig. 9)**. As before, no yielding of the flexural reinforcement in the flange was observed throughout the response. The horizontal displacement in the base joint was even smaller than that in wall W1: only 0.06 mm at failure (**Fig. 11**). This shows once again that the construction joint had an adequate resistance against shear sliding and did not contribute to the global deformations of wall W2. A significant contribution to the global deformations came from the horizontal displacement in the critical diagonal crack as shown in **Fig. 10**. The critical crack in W2 formed earlier than in W1 and reached a horizontal displacement of 2.2 mm at failure (1.6 mm in W1). This large crack displacement shows that the horizontal reinforcement in the precast walls of W2 have yielded prior to failure.

In terms of compressive strains in the CLZ, wall W2 reached slightly smaller values than W1 (see **Fig. 15**). On the other hand, some parts of the CLZ started crushing just before failure (≈96% of peak strength). At failure, the

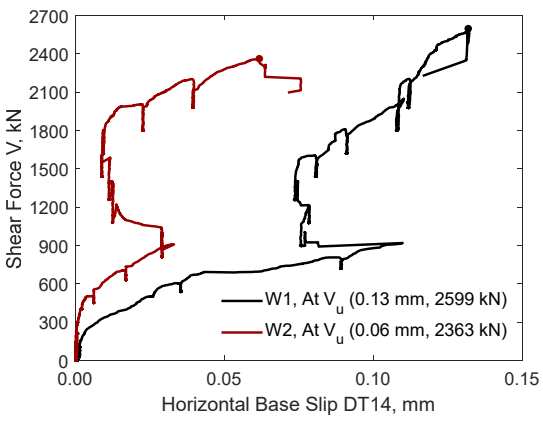

Fig. 11 Measured base crack/joint sliding in walls W1 and W2.

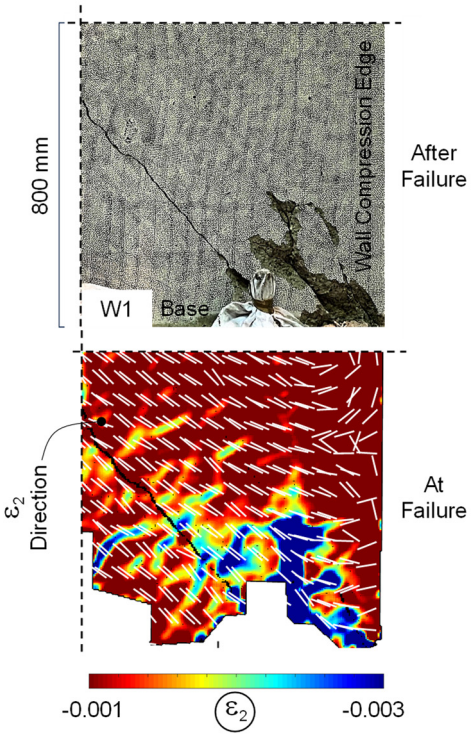

Fig. 12 Contour map of principal compressive strain ε_2 from post-processing of DIC measurements at failure of wall W1 at wall's toe on the flexural-compression side.

principal strains ε_2 exceeded 2.0‰ and localised along the critical diagonal in the bottom ≈500 mm of the height of the wall. These smaller values can be explained in part with potential limited debonding between the precast walls and the core concrete within the CLZ. Because the CLZ has a significant contribution to the shear resistance of squat walls. Such local debonding and/or random variations in the paths of the critical cracks can in turn explain the slight difference (≈9%) in strength between W1 and W2.

4. Kinematics-based analysis from experimental measurements

The deformations in walls W1 and W2 are analysed with the help of the three-parameter kinematic theory (3PKT) (Mihaylov *et al.* 2016) for short shear-dominated walls ($a/h \leq 3.0$). This modelling approach is built on a kinematic description of the deformed shape of the wall, which uses three independent kinematic parameters (degrees of freedom, DOFs). It also includes equilibrium

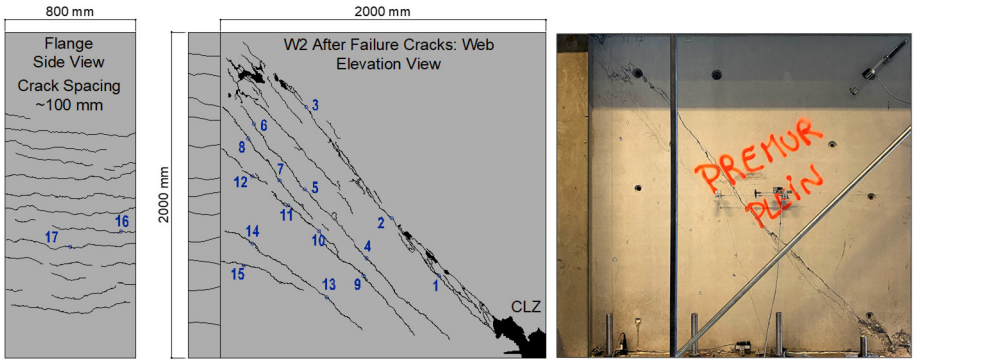

Point	Crack Width, mm Load Level V/V_u, %										
	19	27	34	38	46	53	61	69	76	84	100
1	–	–	–	–	–	–	0.35	0.59	0.60	0.63	1.26
2	–	–	–	–	–	–	0.60	0.93	1.26	1.82	2.21
3	–	–	–	–	–	–	0.37	0.57	0.75	1.09	1.42
4	–	–	–	–	–	0.25	0.34	0.37	0.50	0.59	0.63
5	–	–	–	–	–	0.32	0.49	0.50	0.50	0.50	0.74
6	–	–	–	–	–	0.18	0.25	0.29	0.37	0.45	0.65
7	–	–	–	–	0.10	0.23	0.37	0.36	0.40	0.42	0.46
8	–	–	–	–	0.22	0.24	0.27	0.28	0.33	0.46	0.49
9	–	–	0.31	0.36	0.37	0.38	0.38	0.38	0.42	0.42	0.71
10	–	–	0.30	0.31	0.43	0.46	0.49	0.49	0.50	0.55	0.90
11	–	–	0.20	0.25	0.25	0.27	0.28	0.28	0.28	0.30	0.55
12	–	–	0.13	0.18	0.19	0.24	0.27	0.28	0.33	0.34	0.54
13	–	–	–	–	0.20	0.23	0.28	0.32	0.34	0.35	0.60
14	–	–	–	–	0.15	0.22	0.22	0.22	0.30	0.35	0.58
15	–	–	–	–	–	–	–	0.24	0.25	0.29	0.41
16	0.04	0.07	0.09	0.09	0.09	0.13	0.13	0.13	0.18	0.21	0.30
17	–	–	–	–	0.11	0.18	0.18	0.18	0.22	0.27	0.40

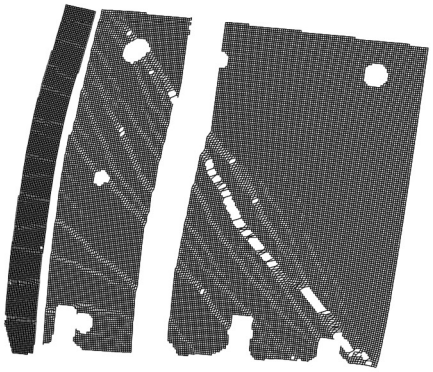

Deformed Shape-At Failure Peak Load
(Scale Factor ×30)

Fig. 13 Crack pattern (major cracks) of wall W2 after failure, crack widths at various load levels, and deformed shape at peak load.

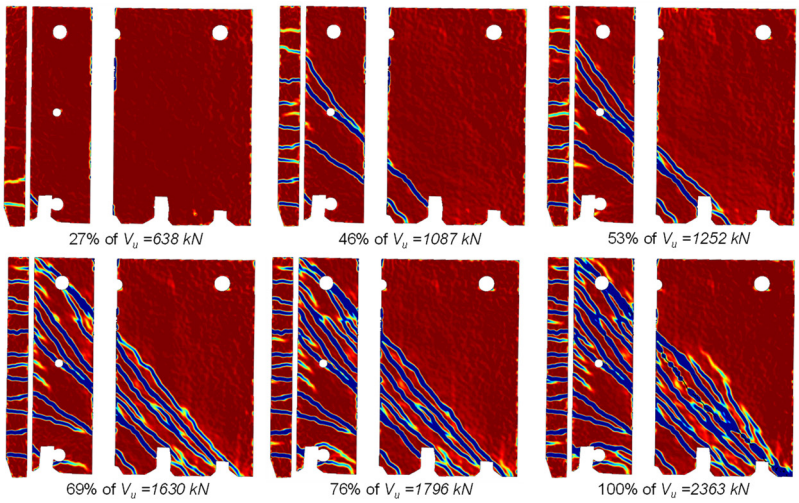

Fig. 14 Contour map of principal tensile strain ε_1 from post-processing of DIC measurements of wall W2.

conditions and constitutive relationships for the mechanisms of shear resistance across critical diagonal cracks. In the following, the experimental data is used to obtain the DOFs of the kinematic model, which are in turn used to quantify the dominant modes of deformations exhibited by the tested walls.

Figure 16 shows the three modes of deformations according to the 3PKT, each of which a function of a single DOF. Additionally, fourth and fifth modes are included in this study to model the opening of the base joint/crack and the elastic shear deformation of the walls, respectively. In the 3PKT, the critical shear crack divides the wall into two regions: a rigid block above the crack and a fan of struts below the crack. The first DOF of the model corresponds to the elongation of the flexural-tension reinforcement (vertical tie), expressed with the average strain along the reinforcement $\varepsilon_{t,avg}$. As DOF $\varepsilon_{t,avg}$ increases, the fan of struts opens, and the rigid block rotates about the toe of the wall (pivot A). Associated with that, the critical shear crack widens.

The second deformation pattern is characterized by the horizontal displacement of the rigid block relative to the fan (DOF Δ_c). This displacement results in widening and slip displacements in the critical shear crack. Additionally, Δ_c is associated with compressive strains and stresses in the critical loading zone in the vicinity of the toe of the wall.

The third DOF is the downward displacement Δ_{cx} occurring in the CLZ, which results in rotation of the rigid block about pivot *B* at the bottom of the vertical tie. DOFs $\varepsilon_{t,avg}$ and Δ_c are sufficient for the modelling of members without axial load or prestressing, while DOF Δ_{cx} is necessary in the presence of axial compression which tends to drive the rigid block downwards. The rotation about pivot B is associated with widening and slip displacements in the critical crack.

The fourth deformation pattern in **Fig. 16** describes the rigid-body rotation of the wall associated with the opening of the base joint/crack. The selected controlling parameter in this mode is the crack opening w_b at the centre of the flexural-tension reinforcement (tie). This crack opening occurs mainly due to the penetration of the reinforcement strains in the foundation block, and the associated pull-out displacement of the reinforcement. As the reinforcement is pulled out of the foundation, the wall rotates around the neutral axis of the base section (point O). The neutral axis is defined by the length of the compression zone *c*.

Finally, the last deformation (fifth) deformation pattern accounts for to the elastic shear strains $\gamma_{el.}$ in the concrete block above the crack, which can be evaluated based on the elastic beam theory in Eq. (1).

$$\gamma_{el.} = f_{sf} \frac{V}{G_c A_c} \tag{1}$$

where the f_{sf} is the form shear factor that depends on the shape of the section (1.51 for W1 and 1.45 for W2) (Gere

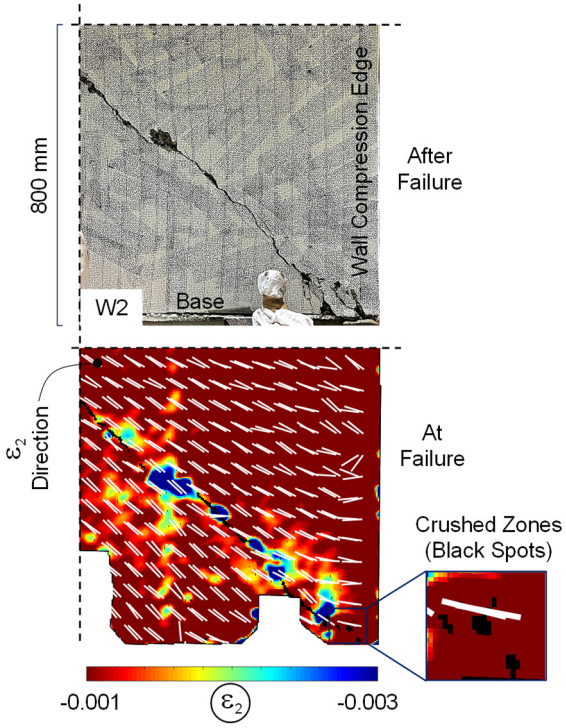

Fig. 15 Contour map of principal compressive strain ε_2 from post-processing of DIC measurements at failure of wall W2 at wall's toe on the flexural-compression side.

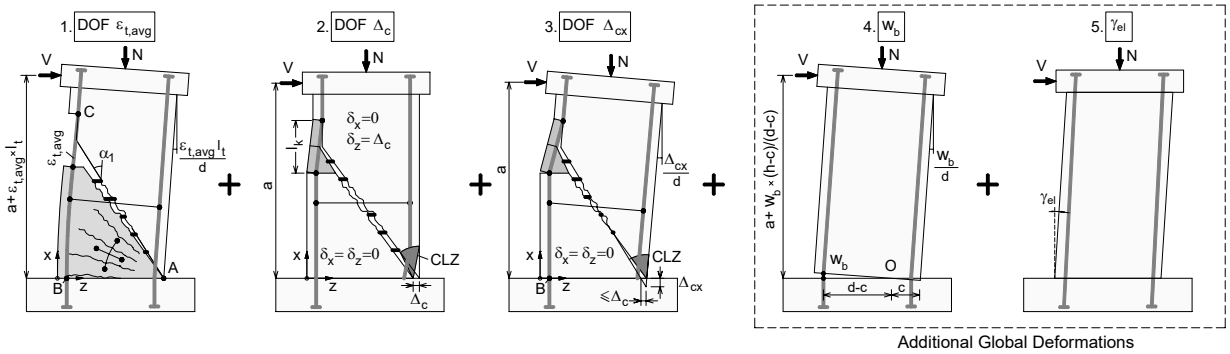

Fig. 16 Three-parameter kinematic model of short shear walls.

and Timoshenko 1984), V is the applied shear force, $G_c \approx 0.4E_c$ is the shear modulus of the concrete, and A_c is the area of the gross concrete section.

By superimposing the five deformation patterns for given values of $\varepsilon_{t,avg}$, Δ_c, Δ_{cx}, w_b, and γ_{el}, the full displacement field and crack displacements can be obtained.

The determination of the kinematic parameters (DOFs) of the test specimens begins with the crack opening w_b at the centre of the tension flange (tie). To obtain the rotation of the wall due to w_b, it is also necessary to estimate the length of the compression zone c. This is achieved by studying the equilibrium of the vertical forces in the base section (see **Fig. 17**). The strain distribution along the section is assumed to be linear (plane sections hypothesis). Additionally, the strains in the tensile flexural reinforcement (tie) are estimated from the base crack opening w_b in combination with Sigrist's bond model (Sigrist 1995). In this bond model, the bond stress along the bar is a function of the tensile strength of the concrete f_{ct}, which is estimated at $0.33f_c'^{1/2}$ (MPa). The bars are assumed anchored in two uncracked concrete blocks, one on each side of the base crack. To this end, the obtained values of w_b for walls W1 and W2 are plotted in **Fig. 18(d)** as functions of the applied load.

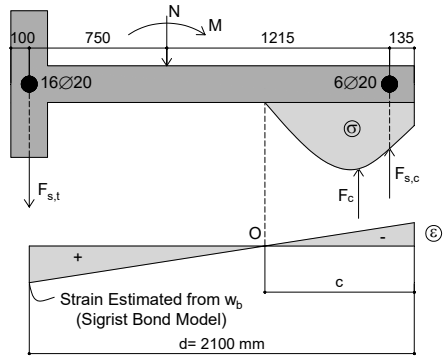

Fig. 17 Estimation of neutral axis depth c from vertical equilibrium at the base section (at peak strength, and with c=approx. 746 mm for both walls).

To obtain DOFs $\varepsilon_{t,avg}$ and Δ_{cx}, it is necessary to use the vertical transducers DT3 and DT4 linking the top and bottom concrete blocks. Due to the rigidity of the blocks, a linear variation is assumed between the displacement readings of the two transducers along the length of the wall (**Fig. 17**). To remove the effect of the base crack, the linear displacements along the crack defined by w_b and c are subtracted from the linear profile obtained from DT3 and DT4. In this way, the readings of DT3 and DT4 are

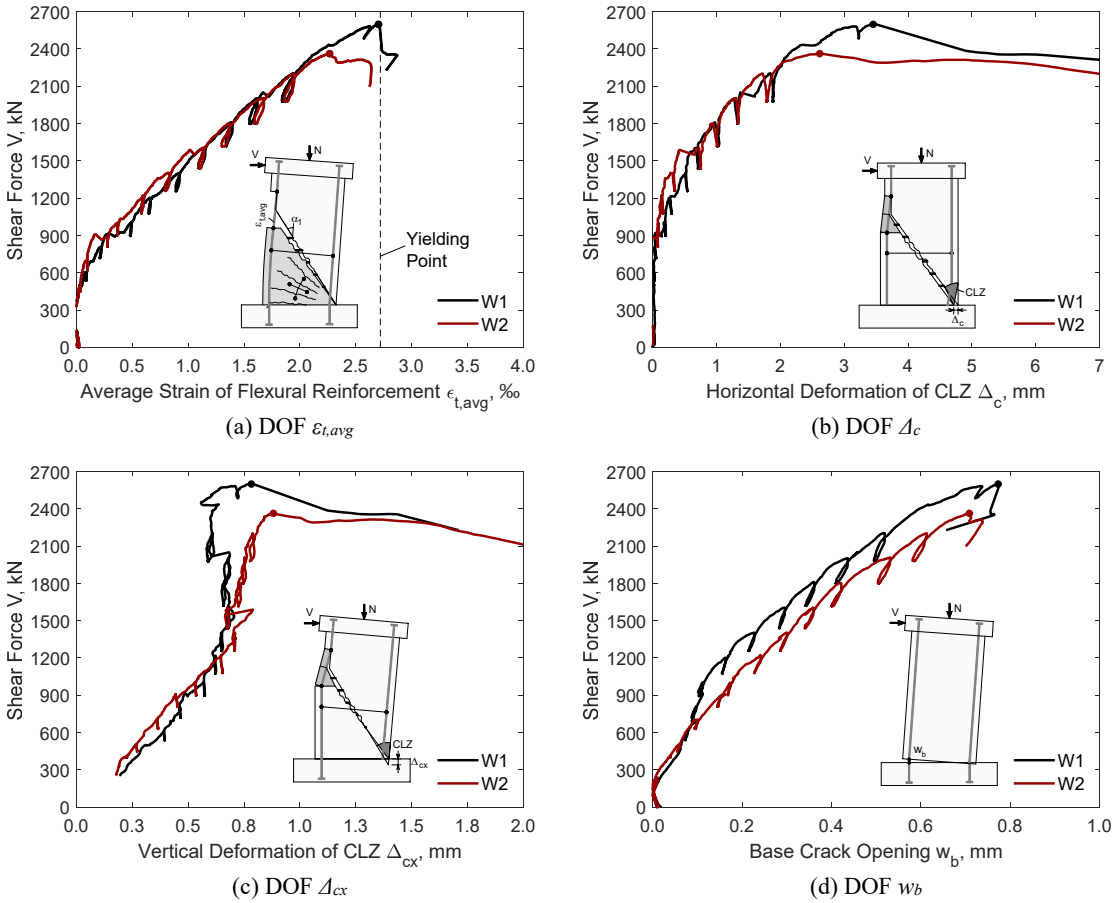

(a) DOF $\varepsilon_{t,avg}$ (b) DOF Δ_c

(c) DOF Δ_{cx} (d) DOF w_b

Fig. 18 Degrees of freedom of kinematic model obtained from test measurements in walls W1 and W2.

Table 3 Degrees of freedom of kinematic model obtained from the test measurements at failure.

Wall	DOFs				
	$\varepsilon_{t,avg}$	Δ_c	Δ_{cx}	w_b	γ_{el}
	‰	mm	mm	mm	‰
W1	2.70	3.45	0.78	0.77	0.57
W2	2.27	2.61	0.88	0.71	0.50

corrected to $DT3_C$ and $DT4_C$, respectively. A linear interpolation between $DT3_C$ and $DT4_C$ allows to determine DOF Δ_{cx} at the compression edge of the wall. Similarly, the elongation of the vertical tie δ_t is obtained by interpolating between $DT3_C$ and $DT4_C$ at the centre of the tension flange of the wall. DOF $\varepsilon_{t,avg}$ is then calculated by dividing δ_t by the length of the tie $l_t=d\times(a_{cl}/h)$, where d is the effective length of the wall measured from the compression edge to the centre of the flange, h is the total wall length, and a_{cl} is the clear height of the wall. The obtained values of $\varepsilon_{t,avg}$ and Δ_{cx} are plotted in **Figs 18(a)** and **18(c)**, respectively, as functions of the applied load on walls W1 and W2.

Finally, DOF Δ_c is obtained on the basis of the horizontal displacement transducer DT5 as in Eq. (2). As the displacement reading by DT5 comes from all five deformation modes in **Fig. 16**, the contributions of kinematic parameters $\varepsilon_{t,avg}$, Δ_{cx}, w_b, and γ_{el} are subtracted from DT5. The term in the brackets is the rotation of the wall associated with $\varepsilon_{t,avg}$, Δ_{cx}, w_b and γ_{el}. The obtained values of Δ_c are plotted in **Fig. 18(b)** as a function of the applied load on walls W1 and W2.

$$\Delta_c = |DT5| - \left(\frac{\varepsilon_{t,avg} l_t}{d} + \frac{\Delta_{cx}}{d} + \frac{w_b}{d-c} + \gamma_{el} \right) a_{DT5} \tag{2}$$

where a_{DT5} is the vertical distance from the location DT5 to the base of the wall.

Table 3 summarizes the values of DOFs $\varepsilon_{t,avg}$, Δ_c, Δ_{cx}, w_b, and γ_{el} at failure. The average strain along flexural reinforcement $\varepsilon_{t,avg}$ reached 2.70‰ and 2.27‰ in W1 and W2, respectively. The yield strain of the reinforcement was 2.70‰, and therefore these results are consistent with the earlier conclusion that the reinforcement remained elastic. It can also be seen that the DOF associated with shear (Δ_c) was approximately 3-4 times larger than Δ_{cx} associated with the action of the vertical load. This is due to the low-aspect ratio ($a/h\approx1.0$) of the walls.

For more direct comparisons of the DOFs of the walls, the contribution of each DOF to the top lateral displacement Δ is evaluated from Eq. (3). This equation is equivalent to Eq. (2), except that a_{DT5} is replaced by the total height of the wall subjected to shear a:

$$\Delta = \Delta_c + \left(\frac{\varepsilon_{t,avg} l_t}{d} + \frac{\Delta_{cx}}{d} + \frac{w_b}{d-c} + \gamma_{el} \right) a \tag{3}$$

The results obtained from Eq. (3) are plotted in **Fig. 19** for the entire response of walls W1 and W2. The plots are presented in an accumulative manner, starting with the shear DOF Δ_c. The largest contribution comes from $\varepsilon_{t,avg}$, followed by Δ_c, w_b, γ_{el}, and Δ_{cx}, respectively. When the five contributions are added up, they capture well the total top displacement Δ with a difference of only ≈5%. **Table 4** summarizes the calculated components of Δ at failure of walls W1 and W2. According to the results, $\varepsilon_{t,avg}$ contributes with ≈45%, Δ_c with ≈27%, w_b and γ_{el} contribute each with ≈10%, and Δ_{cx} with ≈8%.

As shown earlier, the strength of the wall with a pre-wall system W2 was ≈9% lower than that of the cast-in-place wall W1. This can be attributed to several reasons: normal scatter (only 9% difference in strength), random variation in the path of the critical shear crack, and/or limited debonding between the cast-in-place concrete and the precast pre-walls. In the case of the random variation of the path of the critical crack, it was confirmed from the

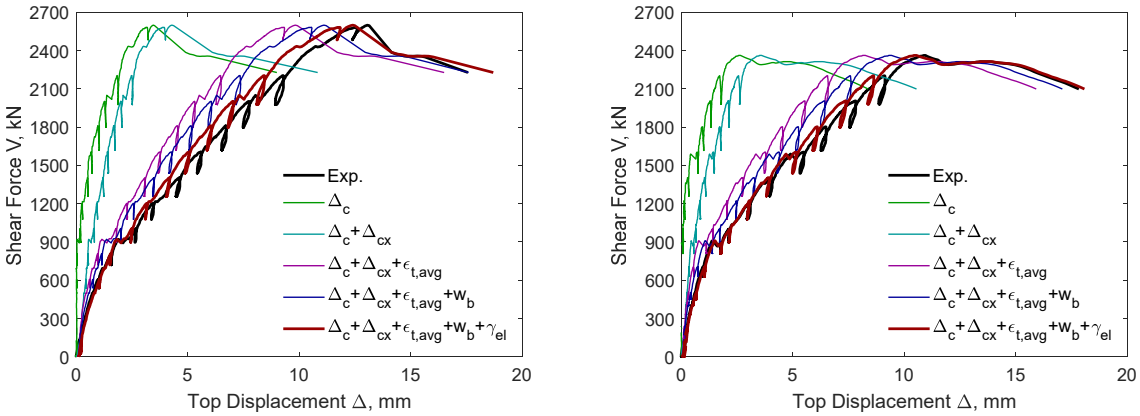

(a) Wall 1 (b) Wall W2

Fig. 19 Components of deformations in walls W1 and W2.

Table 4 Contribution of the DOFs to the top lateral displacement at failure.

Wall	DOFs					Top displacement		
	$\varepsilon_{t,avg}$	Δ_c	Δ_{cx}	w_b	γ_{el}	$\Delta_{kin.}$	$\Delta_{exp.}$	$\Delta_{exp.}/\Delta_{kin.}$
	%	%	%	%	%	mm	mm	-
W1	45	28	7	10	10	12.4	13.0	1.05
W2	44	25	9	11	11	10.5	10.9	1.04

crack patterns that the paths of the critical shear cracks at failure are different for the tested walls. These different paths can change the size of the compression zone (CLZ), where this zone significantly contributes to the total shear carried by the walls. The CLZ is bounded by wall's base, wall's compression edge, and the critical shear crack (see **Figs. 12** and **15**). In case of W1, the critical crack intersects the base of the wall at a distance of 230 mm from the wall's compression edge, while the critical shear crack of W2 intersects at a distance of 100 mm. In other words, the size of the CLZ of W2 is much smaller than the one of W1, which can explain the difference in strength. This can also be clarified from the estimated value of Δ_c of wall W2, which is ≈24% lower than that of W1. Thus, it can be concluded that the primary reason for the difference in the strength of the tested walls is rooted in the random variation in the path of the critical shear crack.

5. Three-parameter kinematic theory (3PKT) predictions of ultimate response

5.1 Summary of original 3PKT method for ultimate response of walls with rectangular sections

Degrees of freedom $\varepsilon_{t,avg}$, Δ_c and Δ_{cx} in **Fig. 16** are linked to the shear strength of short shear walls failing along critical diagonal cracks. This is because these DOFs affect the deformations along the diagonal crack (i.e., crack widths and stirrup strains), as well as the deformations in the critical loading zone (CLZ). The 3PKT method is built on DOFs $\varepsilon_{t,avg}$, Δ_c and Δ_{cx}, and also includes equilibrium conditions and constitutive relationships to predict the ultimate response of short walls with aspect ratio $a/h \leq 3$ (Fathalla and Mihaylov 2022).

In the 3PKT, DOFs Δ_c and Δ_{cx} are calculated in advance, assuming that the concrete in the CLZ crushes when the wall fails in shear. The third DOF, $\varepsilon_{t,avg}$, is calculated by solving the equation of the total shear carried by the resting components in Eq. (4) with the equilibrium equation in Eq. (5).

$$V = V_{CLZ}\left(\Delta_c, \Delta_{cx}\right) + V_{ci}\left(\Delta_c, \Delta_{cx}, \varepsilon_{t,avg}\right) + V_s\left(\Delta_c, \Delta_{cx}, \varepsilon_{t,avg}\right) + V_d\left(\varepsilon_{t,avg}\right) \quad (4)$$

where V_{CLZ} is the shear carried in the CLZ, V_{ci} is the aggregate interlock shear along the critical diagonal crack, V_s is the contribution of the horizontal web reinforcement, and V_d is the shear carried by dowel action of the flexural tension reinforcement.

Shear V_{eq} is obtained from the moment equilibrium of the wall taken about the compression force in the base section as in Eq. (5).

$$V_{eq.} = \begin{bmatrix} E_s A_s \varepsilon_{t,avg} z \\ +N\left[h_N - \left(d - z\right)\right] \end{bmatrix} / a$$
$$z = \min\left[-0.6\frac{N}{f_c' bh} + 0.9, 0.9 \right] d \quad (5)$$

where E_s is the modulus of elasticity of the reinforcement, A_s is the area of the flexural-tension reinforcement, z is the lever arm of the internal vertical forces in the base section of the wall, d is the distance from the centre of the flexural-tension reinforcement to the compressive edge of the wall, and h_N is the distance from the applied axial load N to the compressive edge of the wall.

5.2 Extended 3PKT method for walls with tension flanges

To gain further understanding of the behaviour of squat walls, it is of interest to apply the 3PKT method to walls W1 and W2. To this end, it is necessary to extend the original method for rectangular sections to walls with tension flanges. The presence of a flange modifies the spacing of the flexural-shear cracks s_{cr}, which needs to be estimated in the 3PKT. In this study, s_{cr} is updated in a simple manner (see Appendix) by replacing the effective tension area of rectangular sections $2.5(h\text{-}d)$ with the area of the tension flange in T-sections $B_f t_f$. The crack spacing affects mainly the aggregate interlock shear contribution V_{ci} in terms of crack control factor n_{cr} in the crack displacements calculations.

Moreover, the evaluation of the stresses in the horizontal web reinforcement is enhanced compared to the original 3PKT method. The steel stress f_v is estimated from the horizontal crack displacement w_h halfway along the diagonal crack by using rigid-plastic bond behaviour (Sigrist 1995), as shown in **Fig. 20**. In this model, the bar is considered anchored on each side of the crack and the anchorage length is divided into two segments: l_1 where the reinforcement has yielded and l_2 where the reinforcement is elastic. The bond stress is assumed constant in each segment with values f_{ct} within l_1 and $2f_{ct}$ within l_2 ($f_{ct}=0.33f_c^{0.5}$ MPa). Through bar equilibrium, the relation between bar stress f_v and crack displacement w_h is derived. This relationship is averaged for each value of w_h to account for the fact that the crack displacements decrease towards the bottom and top of the wall. The average

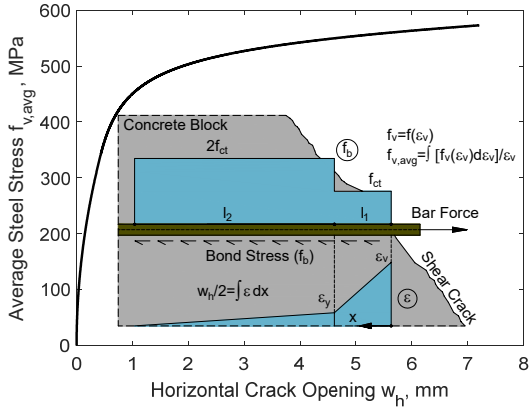

Fig. 20 Predicted average response of web reinforcement with the progress of horizontal crack opening (using average concrete properties f_c=51.75 MPa).

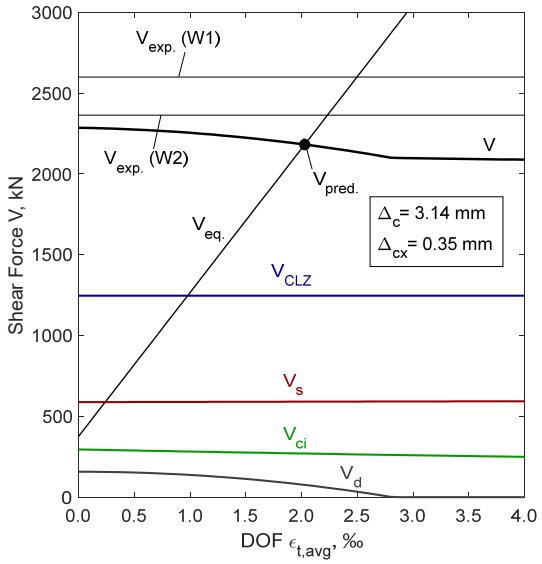

Fig. 21 Graphical solution of 3PKT equations for tested walls.

stress $f_{v,avg}$ is multiplied by the area of the horizontal reinforcement crossing the critical crack to obtain shear component V_s (see Appendix).

As evident from the conducted experiments, the difference between the strength of the cast-in-place wall and the hybrid wall was only 9%. This difference may occur due to several reasons as mentioned earlier in Section 4. Thus, it was decided not to perform any modifications to consider the precast walls in the 3PKT strength calculations. However, in other cases of precast walls with different construction methods where they have a pronounced negative impact on the strength, a reduction factor can be introduced to the strength calculations of the CLZ for the contribution of the precast walls.

5.3 Predictions of extended 3PKT method

Figure 21 shows the graphical solution of Eq. (4) for walls W1 and W2. The predictions are obtained with an average compressive strength of the concrete of 51.75 MPa and using the design dimensions of the walls. The detailed calculations are provided in the Appendix of the paper. DOFs Δ_c and Δ_{cx} are predicted at 3.14 mm and 0.35 mm, respectively, which agree reasonably well with the measured values of Δ_c and Δ_{cx} 2.61-3.45 mm and 0.78-0.88 mm (**Table 3**), respectively. The thin black line represents the left-hand side of Eq. 4, and the thick black line is the shear resistance on the right-hand side of the equation. The solution is obtained at the intersection of the two lines where DOFs $\varepsilon_{t,avg}$ is 2.0‰. This value is also in a reasonable agreement with the measured values of 2.27-2.70‰.

Finally, the shear strength prediction according to **Fig. 21** is 2181 kN for both walls. The corresponding experimental-to-predicted ratios are 1.20 for W1 and 1.08 for W2. Even though the 3PKT neglects the effect of the precast walls, it produces slightly conservative predictions for W2. According to the model, 58% of the shear in the walls was carried in the CLZ, 27% was resisted by the horizontal reinforcement, 12% by aggregate interlock, and only 3% by dowel action of the flexural reinforcement. These results add to the already extensive validation of the 3PKT and show that this approach can be used for assessing the shear strength of both cast-in-place walls and hybrid walls with a pre-wall system (Mihaylov *et al.* 2016; Fathalla and Mihaylov 2022).

6. Conclusions

This study presented experimental research on two full-scale squat shear walls: one conventional cast-in-place wall W1, and one hybrid wall W2 with a pre-wall system (two precast walls) and a cast-in-place core. Apart from the construction method, the two walls were built with nominally identical properties. They were subjected to a constant vertical load and a monotonically increasing lateral load up to shear failure. The following conclusions were reached based on detailed measurements and modelling of the walls with the extended three-parameter kinematic theory (3PKT) for members with tension flanges:

1) The response of the two walls was nearly identical in demonstration of the adequacy of the hybrid method of construction using pre-wall system. The lateral stiffness was unaffected by the precast walls, while the shear strength of wall W2 was only 9% lower than that of W1. Additionally, the hybrid method has proven to provide sufficient anchorage between the wall and the foundation since no sliding was observed during the test up to failure.
2) The deformations in squat walls can be divided in five components associated with different local deformations: average strain in the flexural-tension reinforcement $\varepsilon_{t,avg}$ (flexure), horizontal deformation Δ_c in the critical loading zone (shear), vertical deformation in the CLZ Δ_{cx} (axial load), opening of the base crack due to strain penetration in the foundation w_b, and elastic shear deformations γ_{el}. Even though walls W1 and

W2 were shear critical, 45% of their lateral drift at failure resulted from the flexural strains $\varepsilon_{t,avg}$. The local shear deformation Δ_c accounted for 27%, Δ_{cx} for 8%, w_b for 10%, and γ_{el} for only 10%.

3) Degrees of freedom $\varepsilon_{t,avg}$, Δ_c and Δ_{cx} can be predicted by the extended 3PKT at shear failure. The extended 3PKT method also produced adequate predictions of the shear strength of the two tested walls. Because the extended 3PKT tends to be slightly conservative for cast-in-place walls, it can also be applied without modifications to short walls with precast walls. Alternatively, a reduction factor can be introduced on the shear carried in the critical loading zone where limited debonding of the precast walls can occur near failure.

Acknowledgment

We express our appreciation to Spurgin Leonhart, France for their indispensable collaboration in the completion of this research. Their expertise and assistance were fundamental to the successful execution of our research, particularly in the construction of the test specimens.

References

Adesina, A., (2020). "Recent advances in the concrete industry to reduce its carbon dioxide emissions." *Environmental Challenges*, 1, 100004.

Correlated Solutions, (2023). "*VIC-3D photo processing software* [online]." Irmo, South Carolina: Correlated Solutions Inc. Available from: <https://www.correlatedsolutions.com/vic-3d>.

Fathalla, E. and Mihaylov, B., (2022). "Simplified three-parameter kinematic theory for shear strength of short reinforced concrete walls." *Journal of Advanced Concrete Technology*, 20(8), 507-524.

Gere, J. M. and Timoshenko, S. P., (1984). "*Mechanics of materials*." 2nd ed. Monterey, California: Brooks/Cole Engineering Division.

Greifenhagen, C. and Lestuzzi, P., (2005). "Static cyclic tests on lightly reinforced concrete shear walls." *Engineering Structures*, 27(11), 1703-1712.

Grimaz, S., Maiolo, A., del Fuoco Friuli, D. R. V. and Giulia, V., (2010). "The impact of the 6 April 2009 L'Aquila Earthquake (Italy) on the industrial facilities and lifelines. Considerations in terms of Natech risk." *Chemical Engineering*, 19, 279-284.

Hannewald, P., Bimschas, M. and Dazio A., (2013). "*Quasi-static cyclic tests on RC bridge piers with detailing deficiencies* (Report No. 352)." Zürich: Institute of Structural Engineering, Federal Institute of Technology (ETH Zürich).

Hirosawa, M., (1975). "*Past experimental results on reinforced concrete shear walls and analysis on them* (Kenchiku Kenkyu Shiryo No. 6)." Tokyo: Building Research Institute. (in Japanese)

Huixian, L., Housner, G. W., Lili, X. and Duxin, H., (2002). "*The Great Tangshan Earthquake of 1976* (Report No. EERL2002001)." Pasedena, California: California Institute of Technology.

Ji, X., Cheng, X. and Xu, M., (2018). "Coupled axial tension-shear behavior of reinforced concrete walls." *Engineering Structures*, 167, 132-42.

Kurama, Y. C., Sritharan, S., Fleischman, R. B., Restrepo, J. I., Henry, R. S., Cleland, N. M., Ghosh, S. K. and Bonelli, P., (2018). "Seismic-resistant precast concrete structures: State of the art." *Journal of Structural Engineering*, 144(4), 03118001.

Lefas, I. D., Kotsovos, M. D. and Ambraseys N. N., (1990). "Behavior of reinforced concrete structural walls: Strength, deformation characteristics and failure mechanism." *ACI Structural Journal*, 87(1), 23-31.

Lopes, M. S., (2001). "Experimental shear-dominated response of RC walls. Part II: Discussion of results and design implications." *Engineering Structures*, 23(5), 564-74.

Luna, B. N., (2016). "*Seismic response of low aspect ratio reinforced concrete walls for buildings and safety-related nuclear applications*." Thesis (PhD). State University of New York at Buffalo, USA.

Luna, B. N., Rivera, J. P. and Whittaker, A. S., (2015). "Seismic behavior of low-aspect-ratio reinforced concrete shear walls." *ACI Structural Journal*, 112(5), 593-604.

Magliulo, G., Ercolino, M., Petrone, C., Coppola, O. and Manfredi, G., (2014). "The Emilia Earthquake: Seismic performance of precast reinforced concrete buildings." *Earthquake Spectra*, 30(2), 891-912.

Mihaylov, B. I., Hannewald, P. and Beyer, K., (2016). "Three-parameter kinematic theory for shear-dominated reinforced concrete walls." *Journal of Structural Engineering*, 142(7), 04016041.

Negro, P., Bournas, D. A. and Molina, F. J., (2013). "Pseudo dynamic tests on a full-scale 3-storey precast concrete building: Global response." *Engineering Structures,* 57, 594-608.

Saatcioglu, M., Mitchell, D., Tinawi, R., Gardner, N. J., Gillies, A. G., Ghobarah, A., Anderson, D. L. and Lau, D., (2001). "The August 17, 1999, Kocaeli (Turkey) Earthquake damage to structures." *Canadian Journal of Civil Engineering*, 28(4), 715-737.

Sigrist, V., (1995). "*Zum Verformungsvermögen von Stahlbetonträgern*." Thesis (PhD). Zürich: Federal Institute of Technology (ETH Zürich). (in German)

Toniolo, G. and Colombo, A., (2012). "Precast concrete structures: The lessons learned from the L'Aquila Earthquake." *Structural Concrete*, 13(2), 73-83.

Yin, Y., Wang, F. and Sun, P., (2009). "Landslide hazards triggered by the 2008 Wenchuan Earthquake, Sichuan, China." *Landslides*, 6(2), 139-152.

Appendix 3PKT shear strength calculation for W1 and W2

The details of the 3PKT shear strength calculation (Fathalla and Mihaylov 2022) for W1 and W2 are explained below.

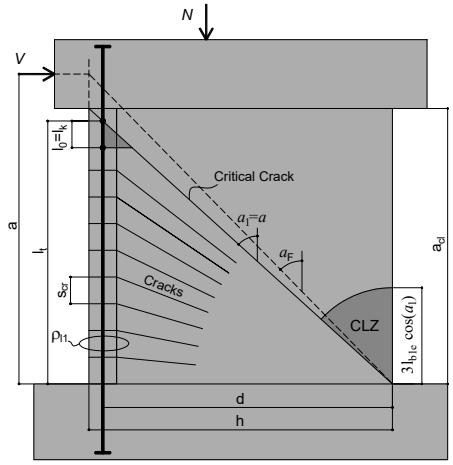

Fig. A1 Geometrical properties of kinematic model.

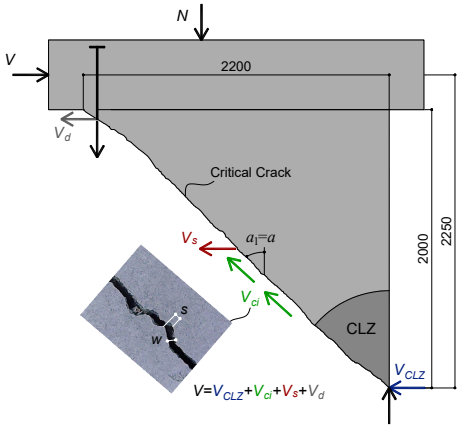

Fig. A2 Shear resisting mechanisms in the 3PKT model.

A.1 Symbols

a	wall height subjected to shear
a_{cl}	wall height subjected to shear
b	width of wall cross-section
B_f	width of the flange in the tension side
t_f	thickness of the flange in the tension side
h	depth of wall section
h_N	distance from axial load to wall edge in compression
d	effective depth of section
d_1	distance from compressive edge of section to furthest tension longitudinal bar
d_b	diameter of main flexural reinforcement
α	angle of wall diagonal with respect to the vertical axis
α_1	angle of critical crack
α_Δ	angle of displacement at CLZ
α_F	angle of force F_{CLZ}
A_s	area of longitudinal reinforcement in one half of the section (tension side)
A_v	area of transverse reinforcement resisting shear
ρ_l	ratio of total longitudinal reinforcement (total area $2A_s$)
$\rho_{l,w}$	ratio of longitudinal web reinforcement
ρ_{l1}	reinforcement ratio in effective tension zone
ρ_v	ratio of transverse reinforcement
a_g	concrete maximum coarse aggregate size
f_c'	cylinder compressive strength of concrete
f_y	yield strength of longitudinal reinforcement
f_{yv}	yield strength of transverse reinforcement
f_v	stress in transverse web reinforcement
$f_{v,avg}$	average stress of the transverse web reinforcement along the diagonal shear crack
l_{b1e}	characteristic length of CLZ
l_t	cracked length along longitudinal reinforcement
l_k	length of transition zone between fan and rigid block
l_0	portion of l_k below the critical diagonal crack
N	axial load
n_b	number of bars corresponding to A_s
n_{cr}	number of major diagonal cracks
s_{cr}	crack spacing in effective tension zone
V	shear force and lateral load
V_{CLZ}	critical loading zone shear resistance
V_{ci}	aggregate interlock shear resistance

V_s transverse reinforcement shear resistance
V_d dowels shear resistance
Δ_c horizontal displacement at CLZ
Δ_{cx} vertical displacement at CLZ
$\varepsilon_{t,avg}$ average strain along longitudinal tension reinforcement
w crack width
s crack slip
w_h horizontal crack opening

A.2 Geometry of the kinematic model

$$\alpha = \tan^{-1}(h / a_{cl}) = \tan^{-1}(2200 / 2000) = 47.7°$$

$$\alpha_1 = \max(\alpha, 30°) = 47.7°$$

$$A_s = \frac{1}{2}\rho_l bh / 100 = \frac{1}{2} \times 2.46 \times 200 \times 2200 / 100 = 5422\,\text{mm}^2$$

$$\rho_{l1} = \frac{A_s}{B_f t_f} \times 100 = \frac{5422}{800 \times 200} \times 100 = 3.4\%$$

Note: B_f of 800 mm is the design value for W1 and W2, not the as built value.

$$s_{cr} = \frac{0.28 \times d_b}{\rho_{l1}} \times 100 = \frac{0.28 \times 20}{3.4} \times 100 = 165\,\text{mm}$$

$$l_0 = \max\left[s_{cr}, \min(1.5(h-d), d - h/2) \cdot \cot\alpha_1\right] = \max\left[165, \min(1.5 \times (2200-2100), 2100 - 2200/2) \cdot \cot 47.7\right] = 165\ \text{mm}$$

$$l_k = l_0 + \min\left[s_{cr}, d \times (\cot\alpha - \cot\alpha_1)\right] = 165 + 0 = 165\ \text{mm}$$

$$l_t = d / \tan\alpha_1 + (l_k - l_0) = 2100 / \tan 47.7 + 0 = 1909\ \text{mm}$$

$$l_{b1e} = \min\left(0.11\sqrt{a^2 + h^2}, 370\right) = \min\left(0.11\sqrt{2250^2 + 2200^2}, 370\right) = 346.2\,\text{mm}$$

$$\alpha_F = \tan^{-1}(h / a) = \tan^{-1}(2200 / 2250) = 44.4°$$

$$\alpha_\Delta = \min\left(\frac{\alpha_F}{\alpha_1} \times 90, 90°\right) = \min\left(\frac{44.4}{47.7} \times 90, 90°\right) = 83.6°$$

$$\because \rho_{lw} \approx 0.2\% \geq 0.2\% \rightarrow n_{cr} = \frac{l_k}{s_{cr}} = 165 / 165 = 1.0$$

A.3 CLZ degrees of freedom Δ_c and Δ_{cx} shear strength contribution V_{CLZ}

$$\Delta_{CLZ} = \frac{\varepsilon_{CLZ} \times 3 l_{b1e} \times \cos\alpha_1}{\cos(\alpha_\Delta - \alpha_F)} = \frac{0.0035 \times 3 \times 346.2 \times \cos 47.7}{\cos(83.6 - 44.4)} = 3.16\,\text{mm}$$

$$\Delta_c = \Delta_{CLZ} \sin\alpha_\Delta = 3.16 \times \sin 83.6 = 3.14\,\text{mm}$$

$$\Delta_{cx} = \Delta_{CLZ} \cos\alpha_\Delta = 3.16 \times \cos 83.6 = 0.35\,\text{mm}$$

$$V_{CLZ} = l_{ble} \times \sin\alpha_1 \times b \times 1.48 f_c'^{0.8} \sin\alpha_F = 346.2 \times \sin 47.7 \times 200 \times 1.48 \times 51.75^{0.8} \sin 44.4 / 1000 = 1245.8\,\text{kN}$$

Note: The compressive strength of the concrete f_c' is the average value for W1 and W2.

A.4 Converged solution at $\varepsilon_{t,avg}$=0.002

$$w = \begin{bmatrix} \left(\dfrac{\varepsilon_{t,avg} l_k h}{2 \cdot \sin\alpha_1 \cdot d}\right) \\ +\Delta_c \cos\alpha_1 \\ +\dfrac{\Delta_{cx}}{d}\left(\dfrac{h}{2\sin\alpha_1} - d\sin\alpha_1\right) \end{bmatrix} / n_{cr} = \begin{bmatrix} \left(\dfrac{0.0020\times 165\times 2200}{2\times\sin 47.7\times 2100}\right) \\ +3.14\times\cos 47.7 \\ +\dfrac{0.35}{2100}\left(\dfrac{2200}{2\times\sin 47.7} - 2100\times\sin 47.7\right) \end{bmatrix} / 1.0 = 2.34\,\text{mm}$$

$$s = \Delta_c \sin\alpha_1 + \Delta_{cx}\cos\alpha_1 = 2.56\,\text{mm}$$

$$w_h = w\cos\alpha_1 + s\sin\alpha_1 = 3.47\,\text{mm}$$

$$\upsilon_{ci} = \frac{0.18\sqrt{f_c'}}{0.31 + 24w/\left(a_g + 16\right)} = \frac{0.18\sqrt{51.75}}{0.31 + 24\times 2.34/\left(16+16\right)} = 0.628\,\text{MPa}$$

$$V_{ci} = \upsilon_{ci}\cdot b\cdot d_1 = 0.628\times 200\times 2148/1000 = 269.6\,\text{kN}$$

$$f_{v,avg}\left(w_h\right)\ \text{Sigrist model} = f_{v,avg}\left(3.47\right) = 534.7\,\text{MPa}$$

$$V_s = \frac{\rho_v}{100} b d_1 \cot\alpha_1 f_{v,avg} = \frac{0.28}{100}\times 200\times 2148\times\cot 47.7\times 534.7/1000$$

$$V_s = 590.4\,\text{kN}$$

$$V_d = n_b\cdot f_y\left[1-\left[\min\left(\frac{\varepsilon_{t,avg}}{f_y/E_s},1\right)\right]^2\right]\times\frac{d_b^{\,3}}{3l_k} = 17.3\times 563\left[1-\left[\min\left(\frac{0.0020}{563/\left(2\times 10^5\right)},1\right)\right]^2\right]\times\frac{20^3}{3\times 165}/1000 = 75.4\,\text{kN}$$

$$V = V_{CLZ} + V_{ci} + V_s + V_d = 1245.8 + 269.6 + 590.4 + 75.4 = 2181\,\text{kN}$$

$$N = 700 + 70 = 770\,\text{kN}$$

Note: The load of approx. 70 kN is added to consider the self-weight of the wall and the weight of the steel assembly on the top block in the test setup (see **Fig. 4**).

$$z = \min\left(-0.6\times\frac{N}{fc'\cdot b\cdot h} + 0.9, 0.9\right)\times d = \min\left(-0.6\times\frac{770\times 1000}{51.75\times 200\times 2200} + 0.9, 0.9\right)\times 2100 = 1847.4\,\text{mm}$$

$$V_{eq.} = \begin{bmatrix} \left(2\times 10^5 A_s \varepsilon_{t,avg}\times z\right) \\ +N\times\left[h_N - \left(d - z\right)\right] \end{bmatrix} / a = \begin{bmatrix} \left(2\times 10^5\times 5422\times 0.0020\times 1847.4\right) \\ +770\times 1000\times\left[1350 - \left(2100 - 1847.4\right)\right] \end{bmatrix} / 2250/1000 = 2181\,\text{kN}$$

$$error = 100\times\left|V_{eq} - V\right| / V_{eq} = 100\times\left|2181 - 2181\right| / 2181 = 0\%$$

$$V_{pred.} = 2181\,\text{kN}$$